Title: Cryo-electron tomography and deep learning denoising reveal native chromatin landscapes of interphase nuclei

Authors: Fadwa Fatmaoui[1], Pascal Carrivain[2], Diana Grewe[3], Burkhard Jakob[4,5], Jean-Marc Victor[2]*, Amélie Leforestier[4]*, Mikhail Eltsov[1]*

Affiliations:

[1]Centre for Integrative Biology (CBI), Department of Integrated Structural Biology, IGBMC, CNRS, Inserm, Université de Strasbourg, Illkirch, France

[2]Laboratoire de Physique Théorique de la Matière Condensée (LPTMC), CNRS, Sorbonne Université, Paris, France

[3]Buchmann Institute for Molecular Life Sciences, Goethe University, Frankfurt am Main, Germany

[4]Department of Biophysics, GSI Helmholtzzentrum für Schwerionenforschung, Darmstadt, Germany

[5]Department of Biology, Techniche Universität Darmstadt, Darmstadt, Germany

[6]Laboratoire de Physique des Solides (LPS), CNRS, Université Paris-Saclay Orsay, France

*Corresponding authors. eltsovm@igbmc.fr; amelie.leforestier@universite-paris-saclay.fr; jean-marc.victor@sorbonne-universite.fr

Abstract:

The folding of nucleosome chains influences DNA availability for functional interactions necessary to the regulation of transcription, DNA replication and repair. Despite models based on *in vitro* studies, the nucleosome chain geometry within the crowded cell nucleus remains elusive. Using cryo-electron tomography and deep learning-based denoising, we directly observed the path of nucleosomal and linker DNA *in situ* in unstained flash-frozen Drosophila embryos. We quantified linker length and curvature characterizing a disordered zig-zag chromatin folding motif, with a low degree of linker bending. Additionally, nucleosome conformational variability with non-canonical structures and sub-nucleosomal particles were seen as individual objects, without structure averaging, highlighting the high structural heterogeneity of native chromatin.

One-Sentence Summary:

Cryo-ET reveals local zig-zag motifs in interphase chromatin, a range of nucleosome conformations, and sub-nucleosomal particles.

Main Text:

Wrapping 145–147 DNA base pairs (bp) around a histone octamer organizes eukaryotic genomes into quasiperiodic arrays of nucleosomes connected by a DNA linker (*1*). Nucleosome arrays behave as flexible heteropolymers capable of folding/unfolding upon interactions between the negatively charged DNA and cations and histone tails enriched in positively charged amino-acids. *In vitro*, nucleosome arrays can fold into regular helical superstructures known as 30 nm fibers, of which two families of models exist: solenoids implying linker bending (*2*) and zig-zags with straight linkers (*3*), with dependence on nucleosome repeat length (NRL (*4*)), nucleosome structure (*5*), and presence/absence of linker histones (*4*). It remains unclear to what extent these models are relevant in the native genome context characterized by variable NRL and DNA sequence, non-uniform binding of linker histones and regulatory proteins, and a highly dynamic nucleosome landscape (*6*). Recent studies describe chromatin as locally disordered (*7*), although high resolution Hi-C experiments and hybrid approaches suggest that local zig-zag and solenoidal folds could exist (*8, 9*).

Nucleosomes and DNA filaments were imaged *in situ* by transmission electron microscopy (EM) in dehydrated, resin-embedded samples (*10-12*). But nucleosome conformation and linker DNA geometry depend on electrostatic contacts that need to be preserved, which is achieved by cryo-immobilization of macromolecules in their native hydrous and ionic environment, followed by cryo-electron tomography (Cryo-ET). Major obstacles in cryo-ET are its low signal-to-noise ratio and anisotropic resolution due to the missing wedge (*13*), especially challenging for small and pleomorphic objects such as nucleosomes and DNA filaments. The conventional solution, sub-tomogram averaging (STA), has revealed nucleosome structure *in situ* at about 20 Å resolution (*14, 15*), but it is not efficient for the variable and flexible DNA linkers. In this study, we explore the chromatin landscape in interphase nuclei by cryo-ET of vitreous sections using contrast enhancement by Volta Phase Plates (VPP), well adapted for DNA visualization and nucleosome analysis (*16*), coupled to deep learning-based denoising independent on structure averaging (*17*).

We chose the central nervous system (CNS) of *Drosophila* embryos at late developmental stages (*13–15*) as a model system, since it presents many practical advantages: entire embryos can be vitrified by high pressure freezing (*18*); a large relative area is occupied by diploid nuclei that accounts for approximately 50% of the total tissue section area (Fig. 1A; Fig. S1), facilitating tomographic data collection. Additionally, as shown by freeze-substitution, CNS nuclei reveal the

stereotypical organization of *Drosophila* embryo chromatin domains (Fig. 1A): compact constitutive heterochromatin (cHC) is attached to the nuclear envelope and associated with the nucleolus (NO), while more dispersed (*18*) domains of euchromatin (EC) and facultative heterochromatin (fHC) are distributed within the nucleosplasm, allowing us to distinguish cHC from ECfHC and target these chromatin compartments.

We recorded VPP cryo-tomograms on 75 nm thick vitreous sections (Fig. S1). Tomogram reconstructions present a granular disordered aspect typical of chromatin (Fig. 1B; Fig. S2A). Zooming in reveals nucleosomes, barely visible in raw reconstructions (Fig. S2B, *raw*), but unambiguously identified after denoising (Fig. 1C, S2B, right panels) with their typical wrapping of two DNA gyres around the histone octamer. This interpretation is supported by STA of manually picked particles from two ECfHC reconstructions (ECfHC1, 549 particles; ECfHC2; 552 particles) and one cHC reconstruction (860 particles), resulting in a 3D nucleosome structure at 13.6 Å resolution in ECfHC1 and 2, and 12.9 Å in cHC (Fig. 1D; Fig. S3; Movie S2). Fitting the x-ray atomic model of the *Drosophila* nucleosome core particle (pdb:2PYO) shows that subtomogram averages are very similar to the canonical nucleosome conformation (Fig. 1D; Fig. S3). However, for individual nucleosomes, our tomograms reveal rich conformational variability. Round top views of nucleosomes demonstrate “open” and “closed” conformations (Fig. 1E). Closed conformations with DNA crossing at nucleosome entry/exit site can occur due to chromatin folding fluctuations or presence of bound linker histones, resulting in a chromatosome (*19*). Open configurations show DNA entry and exit points at a distance larger than in canonical x-ray models, revealing nucleosome breathing *(20, 21) in situ* (Fig.1E, *open*). Further, side views show intergyre distance variation (Fig.1E, *gaping*), compatible with gaping, i.e., edge opening of the nucleosome, in agreement with FRET experiments *in vitro* (*22*) and our previous findings *in situ (15).* The efficiency of signal restoration by denoising is highest in regions of lower local crowding, at the chromatin domain periphery. There, the complete path of DNA wrapped around the histone octamer may be followed around individual nucleosomes (Fig.1F; Movie S3). Beside nucleosomes, other molecular complexes such as chaperonins and proteasomes are readily recognized in the nucleoplasm (Fig. 1B, yellow arrow; Fig. S2B).

Importantly, denoising reveals DNA linkers connecting nucleosomes (Fig. 1C, blue arrows). The best visibility is obtained by the deep-learning network Warp (*23*), but linkers are also revealed by TOPAZ (*24*), and nonlinear anisotropic diffusion (NAD) filter (*25*) (Fig. S2B, Movie S1),

supporting that these linear densities are *bona fide* DNA linkers, not deep-learning artefacts. Linker densities are present in raw reconstructions, although difficult to discern directly: they can be emphasized by averaging voxels along the linker path, once identified in denoised volumes (Fig. S4).

Visualization of DNA linkers allows us to explore their geometry. In optimal situations, the complete linker between two nucleosomes can be traced (Fig. 2A, Movie S4). This class of linkers is hereafter named *2N*. In 46% of the visible linkers (Table S1), only one linked nucleosome can be identified. The linker may end within or close to a density that cannot be assigned to a recognizable nucleosome (Fig. 2B, Movie S5). It could be another unknown macromolecular complex interacting with chromatin, or correspond to an artefactual density overlap of the tomographic reconstruction (*26*). The linker may also turn abruptly untraceable. Simulated tomograms of synthetic chromatin (Fig. S11) demonstrate a local variability in the linker path restoration upon denoising, depending on the signal to noise ratio and on chromatin crowding, with partial or even complete loss of the signal in crowded regions, in good agreement with the situation observed in real data. We combined all cases where the complete linker length was not defined into class *1N*. We also observed situations where the DNA linker was too short to be traced: successive nucleosomes are then in contact, and DNA can be followed passing from one histone core to the other (Fig. 2C, *linker-less*). Traceable linkers correspond to about 13 % of the amount expected from the number of manually picked nucleosomes (Table S1). Worm-like chain (WLC) models (*27*) with a chain unit of 1bp and a persistence length of 50 nm were fitted into the traced linkers. Best fits were processed to calculate linker length and curvature for the *2N* class, curvature only for the *1N* class. The Kolmogorov–Smirnov (KS) test showed no significant difference between linker length and curvature in ECfHC and cHC (Table S2); all data are therefore merged in Figure 2D-E. Distributions for each chromatin domain are shown in Figure S6. The mean linker length is 30 bp (SD 15 bp, Fig. 2D), in agreement with previous measurements of 25–40 bp obtained using micrococcal nuclease digestion followed by gel migration and/or sequencing in Drosophila cells and larvae (*28, 29*). Nevertheless, linkers lengths up to 76 bp and down to a few bp (Fig. 2C) are observed, revealing a large local variability.

Linker curvature is generally low (mean ~ 0.10 nm^{-1}, SD 0.01 nm^{-1}, Fig. 2E). To compare our *in situ* measurements with zig-zag and solenoid models, we simulated their minimal structural motif as di-nucleosomes with stacking interaction for solenoids (with higher curvature) and non-

interacting nucleosomes for zig-zags (Fig. S7). We observed an agreement between the curvature distribution of our experimental data and that of zig-zag models (Fig. 2E; Fig. S8). To test for a possible bias of the denoising algorithm towards preferential recovery of low-curvature straight linkers, we simulated noisy tomograms containing crowded di-nucleosomes with straight and bent linkers (Fig. S11). We found that both situations have the same signal-to-noise ratio threshold for signal recovery and traceability (0.25; Fig. S11). In addition, the distribution of the linker "end-to-end" vector directions within the section's volume show no statistically significant difference from an isotropic distribution (Fig. S10), indicating the absence of substantial cutting-induced deformations at the scale of DNA linker. Taken together our results argue against a widespread solenoidal fold and suggest a zig-zag chromatin geometry, both in ECfHC and cHC. In agreement, wherever two consecutive linkers are visualized, they show zig-zag motifs (Fig. 3A and B).

Judging from our observations, a "disordered zig-zag" (Fig. 3C, Movie S6), evocative of the conformations found by Bednar et al. in solutions of oligonucleosomes (*30*), with variable linker length and lack of extensive order (see for example Fig. 1B and C; Fig. 3A) is a reasonable model of chromatin folding in interphase nuclei. Indeed, we found no correlation between linker length and curvature, indicating a freely-fluctuating DNA and an absence of geometric constrains like stacking. This organization minimizes energy penalties for linker bending (*31*); it is compatible with the high dynamics of nucleosomes at the local scale and interdigitation of neighboring fibers leading to molten globule-like domains (*7*).

Besides nucleosomes and linker DNA, we detected unusual nucleosome-derived particles. Single or triple DNA gyres are observed curved around histone-like densities (Fig. 4). In top views, they are similar to nucleosomes, while side views reveal the single/triple DNA wrapping. Single gyre particles typify sub-nucleosomes, such as tetrasomes and hemisomes documented *in vitro* and *in silico* (*32, 33*). Although the resolution is not sufficient to determine the histone content, different species can be distinguished, with histone-like densities restricted to the region of maximum DNA curvature and missing densities near the DNA entry/exit site (Fig. 4A and B), or more homogeneous repartitions resembling nucleosome halves (Fig. 4C). Atomic models of tetrasomes (H3–H4 tetramers) and hemisomes (one copy of each histone) (*32*) could be fitted within. The triple gyre nucleosome-like particle is similar to the previously described overlapping dinucleosomes (*34*), in which an octasome contacts a hexasome (lacking one histone dimer), as shown by the good fit of its crystallographic structure (pdb: 5GSE) into our volume data (Fig. 4D,

Movie S7). Many of these non-octameric particles were detected as pairs, either of two sub-nucleosomes (Fig. 4B and C) or of an overlapping nucleosome with a sub-nucleosome (Fig. 4D). Interestingly these structures were only found in ECfHC nanodomains; although we cannot discriminate between EC and fHC, we hypothesize they form in EC domains, in agreement with active nucleosome assembly–disassembly and sliding occurring during transcription (*35, 36*). The observation of these labile states *in situ* highlights the potential of denoising-enhanced cryo-ET to address functionally-relevant chromatin reorganization directly in the context of cell nucleus.

Acknowledgments:

We thank W. Hagen for help with data collection at the EMBL in Heidelberg, Germany. We are grateful to J. Dubochet for inspiring discussions, and J. Dubochet and P.Schultz for critical reading of the manuscript. We thank H. Gnaegi (Diatome) for providing diamond knives for vitreous cryo-sectioning, Mohamad Harastani and Slavica Jonic (IMPMC, Paris) for support with subtomogram averaging. ME and DG thank A. Frangakis for providing the laboratory space and access to the equipment. FF and ME were supported by Centre for Integrative Biology (CBI), CNRS, Inserm, University of Strasbourg, and by the French Infrastructure for Integrated Structural Biology (FRISBI ANR-10-INSB-005) and Instruct-ERIC.

Funding:

French National Research Agency (ANR-20-CE11-0020-01 to AL, ANR-20-CE11-0020-02 to ME, ANR-20-CE11-0020-04 to JMV)

German Research Foundation (DFG EL 861/1 to ME)

German Federal Ministry of Education and Research (BMBF 02NUK054A to BJ)

Author contributions:

Conceptualization: ME, AL, FF

Methodology: ME, AL, JMV, FF, PC, DG

Investigation: FF, PC, DG, ME, AL, JMV

Formal analysis: PC, JMV

Funding acquisition: ME, AL, JB

Supervision: ME

Writing – original draft: ME, AL, FF, JMV, PC

Writing – review & editing: ME, AL, FF, JMV, PC, JB

Competing interests: Authors declare that they have no competing interests.

Data and materials availability: Electron density maps for subtomogram averages of nucleosomes were deposited in the Electron Microscopy Data Bank (EMD-15480, EMD-15481, EMD-15483). The data that support the findings of this study are available from the corresponding author upon reasonable request.

Supplementary Materials

Materials and Methods

Supplementary Text

Figs. S1 to S11

Tables S1 to S4

References (*37*–*63*)

Movies S1 to S9

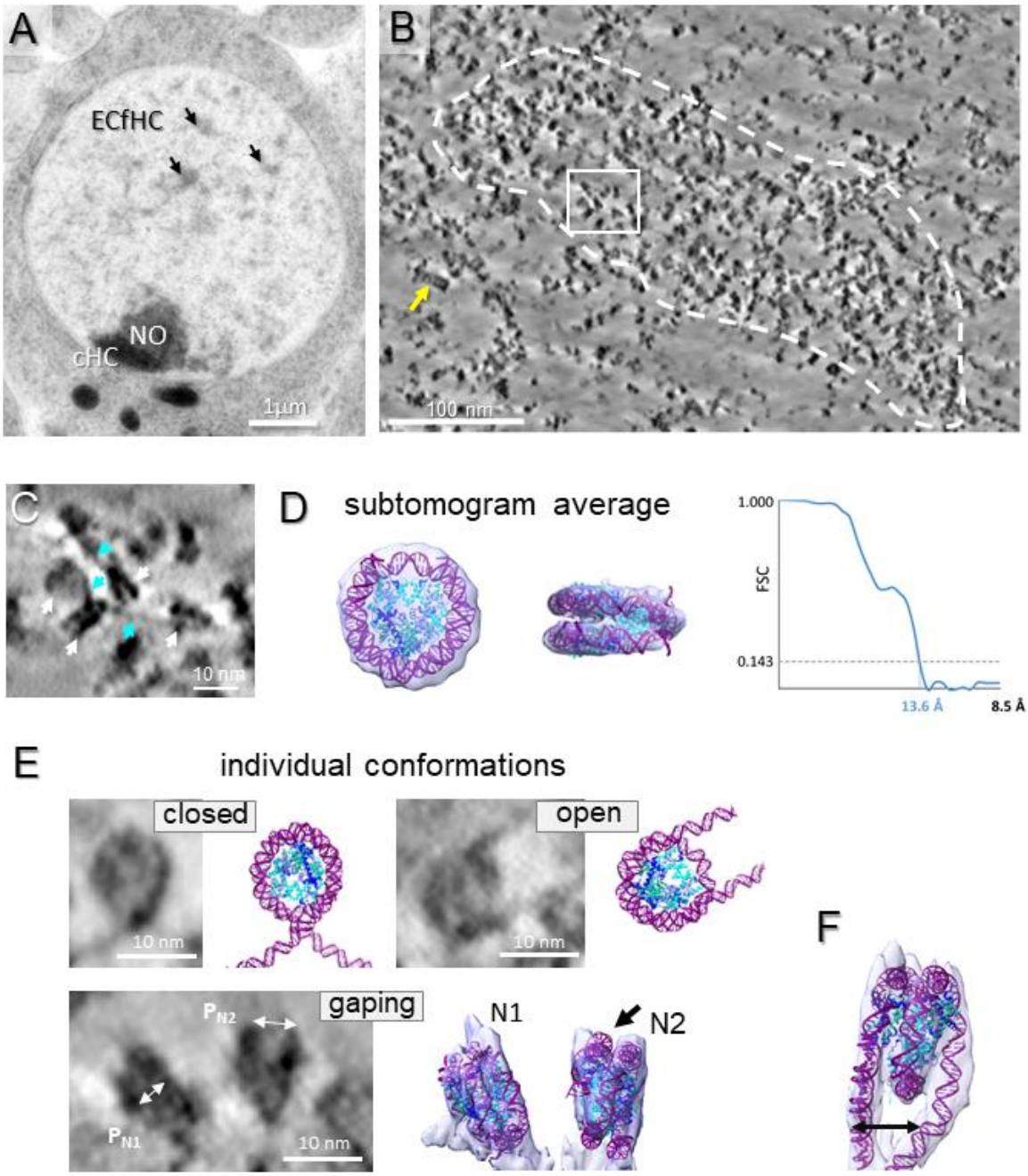

Fig. 1. Chromatin visualization enhanced by computational denoising. (**A**) A section of freeze-substituted embryonic CNS nucleus shows constitutive heterochromatin domain (cHC), nucleolus (NO), and dispersed chromatin domains (arrows) containing ECfHC. (**B**) One voxel (4.25 Å) thick tomographic slice of a cryo-tomogram containing an ECfHC domain. Nucleosomes, 23S proteasomes (yellow arrow) and other macromolecular complexes (see Fig. S2) are well identified after denoising. (**C**) Magnified area from (**B**) showing nucleosomes (white arrows) and linker

DNA (blue arrows). (**D**) Top and two side views of the subtomogram average of manually picked nucleosomes from the ECfHC tomogram (**B**), into which the crystallographic model of the nucleosome (pdb:2PYO) was fitted. Fourier Shell Correlation (FSC) curve showing a 0.143 cutoff at 13.6 Å. (**E**) Individual nucleosomes after Warp denoising. Circular top views with a closed and an open conformation are shown side by side with corresponding models. Side views of two neighboring nucleosomes N1 and N2 showing a difference in their intergyral distances (P) are represented in (gaping). P_{N1} is very close to that of the canonical nucleosome (~ 2.7 nm) whereas P_{N2} is larger (~ 4.0 nm); the x-ray model (pdb:2PYO) fits poorly in N2 (arrow in isosurface). (**F**) Visualization of the complete wrapping of DNA around the histone core. This nucleosome shows a larger lateral spacing between DNA entry and exit sites (double arrow).

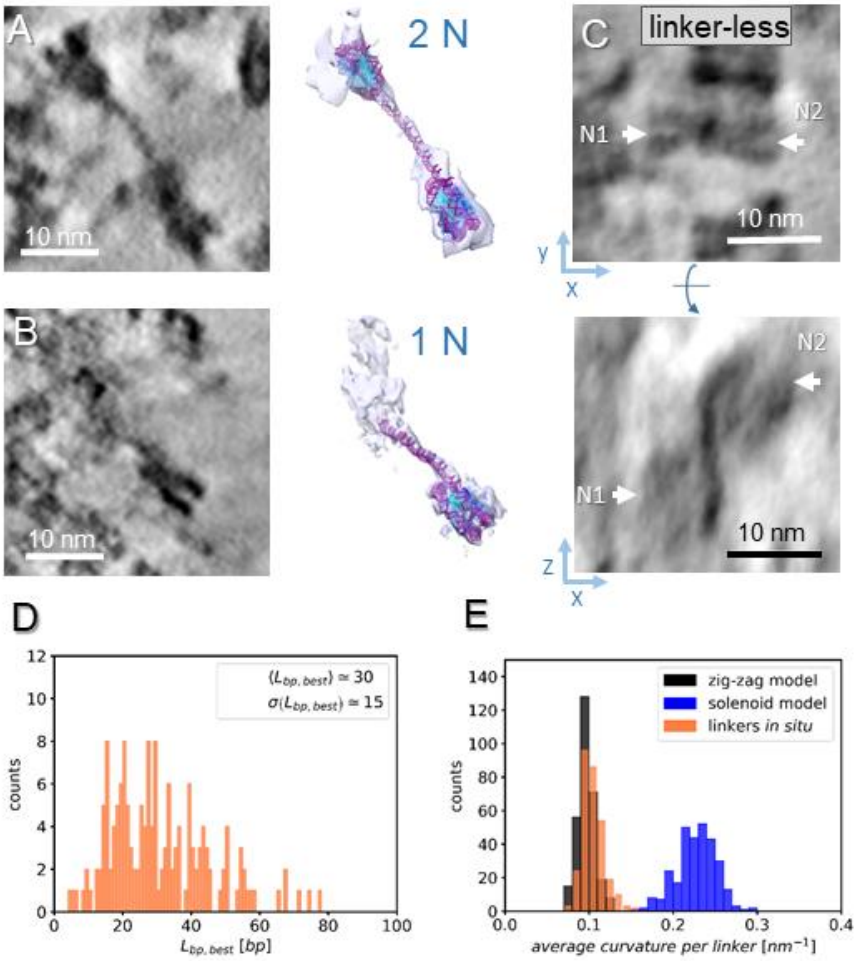

Fig. 2. Analysis of DNA linker length and curvature. (**A, B**) Examples of DNA traced between two successive nucleosomes (2N class, **A**) or from one nucleosome only (1N, **B**) shown as one voxel (4.25 Å) tomographic slices and as isosurfaces with fitted molecular models. (**C**) Example of a linker-less dinucleosome (arrows) shown in side (XY) and top (XZ) views. (**D**) Linker length distribution for the 2N class on nucleosomes. (**E**) Curvature distribution for all traced linkers (orange). The curvature distributions calculated for the solenoid (blue) and the zig-zag (dark grey) models with the same number of linkers are superimposed.

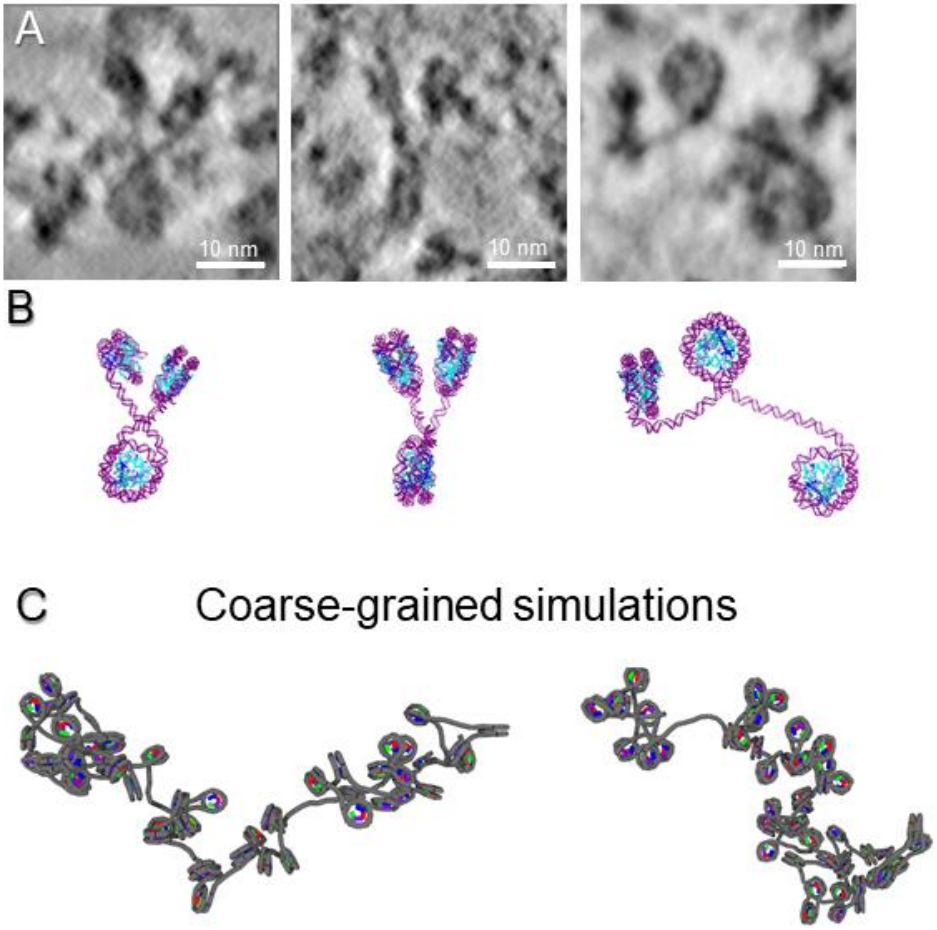

Fig. 3. Zigzag chromatin folding *in situ*. (**A**) Representative 4.25 Å thick tomographic slices illustrating the variety of zig-zag motifs drawn by three successive nucleosomes. (**B**) Molecular models showing our interpretations of views in (**A**). (**C**) Two snapshots of coarse-grained simulations incorporating the measured linker length distribution.

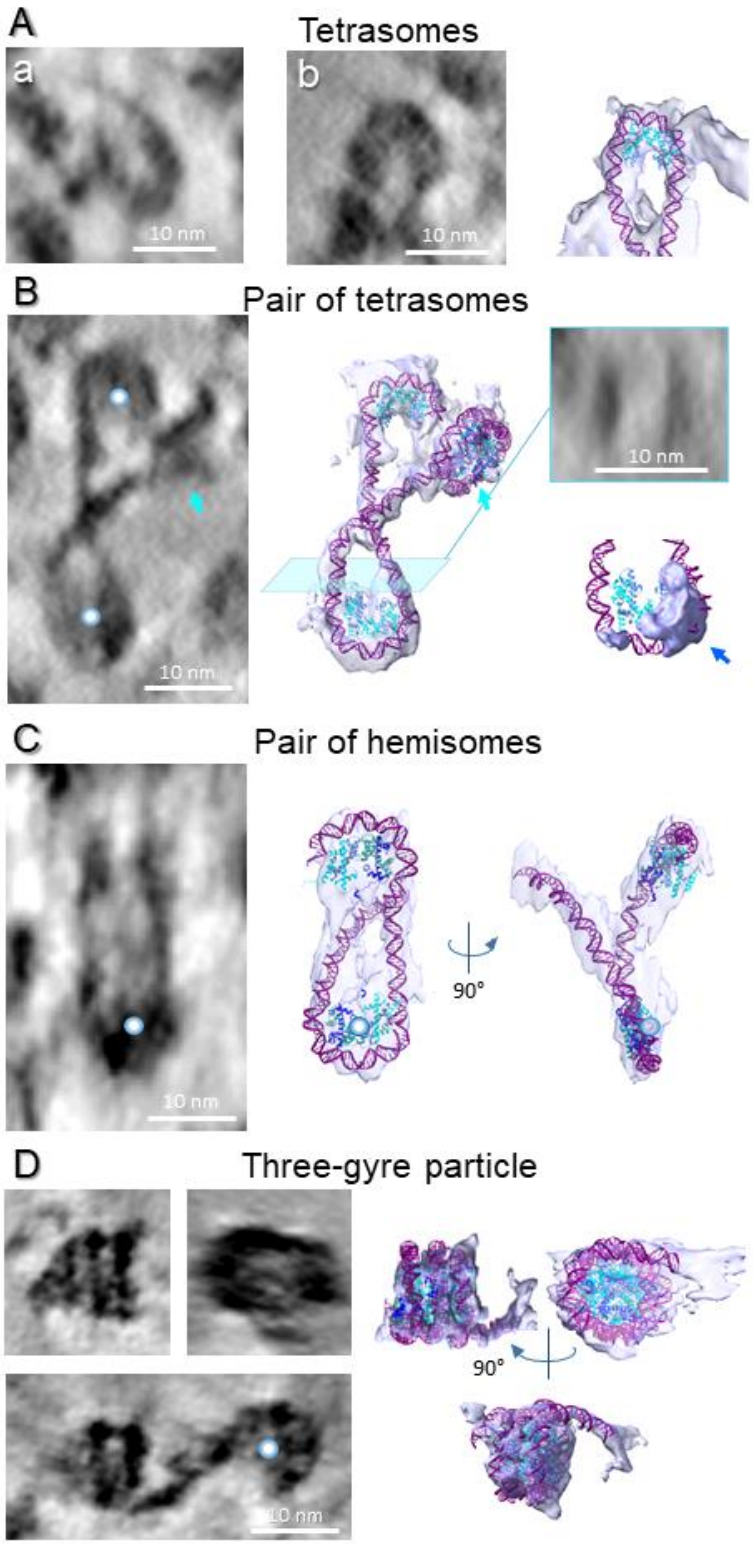

Fig. 4. Evidence for unusual nucleosomes in ECfHC domains. (**A, B**) Sub-nucleosome particles missing histone densities at the DNA entry/exit site and formed by a single DNA loop. Simulated atomic model of a tetrasome fitted into the density shown in **A(b)**. (**B**) Zig-zag fold formed by two

successive tetrasome-like sub-nucleosomal particles (core marked by blue spheres) and a canonic nucleosome (cyan arrow), shown as a tomographic slice and isosurfaces with fitted models. The transverse tomographic section (inset) corresponding to the blue plane demonstrates that the particle is formed by a single DNA loop. This particle shows an additional density attached to DNA oriented perpendicular to the plane of the DNA loop (blue arrow, Movie S6). (**C**) A pair of hemisomes, corresponding to a split nucleosome with its two halves is represented as a tomographic slice and isosurface with fitted nucleosome and DNA models. The blue spheres indicate the same hemisome in the tomographic slice and models (see also Movie S7). (**D**) Three-gyre particle shown as tomographic slices of side and top views and as isosurface views with the fitted model of the overlapping nucleosome (pdb:5GSE). The third modelled DNA gyre does not fully fit the density, indicating conformational difference *in situ.* Oblique virtual section showing its connection to a sub-nucleosomal (tetrasome-like) particle (blue sphere).

References

1. D. E. Olins, & Olins, A. L., Nucleosomes: the structural quantum in chromosomes. *American Scientist* **66**, 704-711 (1978).
2. P. J. J. Robinson, L. Fairall, V. A. T. Huynh, D. Rhodes, EM measurements define the dimensions of the "30-nm" chromatin fiber: evidence for a compact, interdigitated structure. *Proc Natl Acad Sci USA* **103**, 6506–6511 (2006).
3. T. Schalch, S. Duda, D. F. Sargent, T. J. Richmond, X-ray structure of a tetranucleosome and its implications for the chromatin fibre. *Nature* **436**, 138–141 (2005).
4. A. Routh, Sandin, S., & Rhodes, D, Nucleosome repeat length and linker histone stoichiometry determine chromatin fiber structure. *Proc. Natl. Acad. Sci. USA* **105**, 8872-8877 (2008).
5. Y. Takizawa, Ho, C. H., Tachiwana, H., Matsunami, H., Kobayashi, W., Suzuki, M., ... & Kurumizaka, H., Cryo-EM structures of centromeric tri-nucleosomes containing a central CENP-A nucleosome. *Structure* **28**, 44-53 (2020).
6. S. Baldi, P. Korber, P. B. Becker, Beads on a string-nucleosome array arrangements and folding of the chromatin fiber. *Nat Struct Mol Biol* **27**, 109–118 (2020).
7. K. Maeshima, S. Ide, M. Babokhov, Dynamic chromatin organization without the 30-nm fiber. *Curr Opin Cell Biol* **58**, 95–104 (2019).
8. M. Ohno, T. Ando, D. G. Priest, V. Kumar, Y. Yoshida, Y. Taniguchi, Sub-nucleosomal Genome Structure Reveals Distinct Nucleosome Folding Motifs. *Cell* **176**, 520-534.e25 (2019).
9. V. I. Risca, S. K. Denny, A. F. Straight, W. J. Greenleaf, Variable chromatin structure revealed by in situ spatially correlated DNA cleavage mapping. *Nature* **541**, 237–241 (2017).
10. H. D. Ou *et al.*, ChromEMT: Visualizing 3D chromatin structure and compaction in interphase and mitotic cells. *Science* **357**, eaag0025 (2017).
11. L. M. Rapkin, D. R. P. Anchel, R. Li, D. P. Bazett-Jones, A view of the chromatin landscape. *Micron* **43**, 150–158 (2012).
12. C. Kizilyaprak, D. Spehner, D. Devys, P. Schultz, In Vivo Chromatin Organization of Mouse Rod Photoreceptors Correlates with Histone Modifications. *PLOS ONE* **5**, e11039 (2010).
13. M. Turk, W. Baumeister, The promise and the challenges of cryo-electron tomography. *FEBS Letters* **594**, 3243-3261 (2020).
14. S. Cai, Böck, D., Pilhofer, M., & Gan, L, The in situ structures of mono-, di-, and trinucleosomes in human heterochromatin. *Molecular biology of the cell*. **29**, 2450–2457 (2018).
15. M. Harastani, Eltsov, M., Leforestier, A., & Jonic, S., HEMNMA-3D: Cryo Electron Tomography Method Based on Normal Mode Analysis to Study Continuous Conformational Variability of Macromolecular Complexes. *Frontiers in molecular biosciences*. **8** (2021)..
16. E. Y. D. Chua, V. K. Vogirala, O. Inian, A. S. W. Wong, L. Nordenskiöld, J. M. Plitzko, R. Danev, S. Sandin, 3.9 Å structure of the nucleosome core particle determined by phase-plate cryo-EM. *Nucleic Acids Res*. **44**, 8013–8019 (2016).
17. J. Lehtinen *et al.*, Noise2Noise: Learning Image Restoration without Clean Data. *ArXiv* **abs/1803.04189**, (2018).
18. M. Eltsov, D. Grewe, N. Lemercier, A. Frangakis, F. Livolant, A. Leforestier, Nucleosome conformational variability in solution and in interphase nuclei evidenced by cryo-electron microscopy of vitreous sections. *Nucleic Acids Research*. **46**, 9189–9200 (2018).
19. J. J. Hayes, D. Pruss, A. P. Wolffe, Contacts of the globular domain of histone H5 and core histones with DNA in a "chromatosome". *Proc Natl Acad Sci U S A* **91**, 7817-7821 (1994).
20. R. Buning, J. van Noort, Single-pair FRET experiments on nucleosome conformational dynamics. *Biochimie* **92**, 1729-1740 (2010).
21. S. Bilokapic, M. Strauss, M. Halic, Histone octamer rearranges to adapt to DNA unwrapping. *Nat Struct Mol Biol* **25**, 101-108 (2018).
22. T. T. Ngo, T. Ha, Nucleosomes undergo slow spontaneous gaping. *Nucleic Acids Res* **43**, 3964-3971 (2015).
23. D. Tegunov, P. Cramer, Real-time cryo-electron microscopy data preprocessing with Warp. *Nat Methods* **16**, 1146-1152 (2019).
24. T. Bepler, K. Kelley, A. J. Noble, B. Berger, Topaz-Denoise: general deep denoising models for cryoEM and cryoET. *Nat Commun*. **11**, 5208 (2020).

25. A. S. Frangakis, R. Hegerl, Noise Reduction in Electron Tomographic Reconstructions Using Nonlinear Anisotropic Diffusion. *Journal of Structural Biology* **135**, 239-250 (2001).
26. B. Turonova, L. Marsalek, P. Slusallek, On geometric artifacts in cryo electron tomography. *Ultramicroscopy* **163**, 48-61 (2016).
27. M. Doi, S. F. Edwards, *The Theory of Polymer Dynamics*. (New York: Oxford University Press, 1988).
28. X. Lu *et al.*, Linker histone H1 is essential for Drosophila development, the establishment of pericentric heterochromatin, and a normal polytene chromosome structure. *Genes Dev* **23**, 452-465 (2009).
29. S. Baldi, S. Krebs, H. Blum, P. B. Becker, Genome-wide measurement of local nucleosome array regularity and spacing by nanopore sequencing. *Nat Struct Mol Biol* **25**, 894-901 (2018).
30. J. Bednar, R. A. Horowitz, J. Dubochet, C. L. Woodcock, Chromatin conformation and salt-induced compaction: three-dimensional structural information from cryoelectron microscopy. *J Cell Biol* **131**, 1365-1376 (1995).
31. T. Brouwer *et al.*, A critical role for linker DNA in higher-order folding of chromatin fibers. *Nucleic Acids Research* **49**, 2537-2551 (2021).
32. J. Zlatanova, T. C. Bishop, J. M. Victor, V. Jackson, K. van Holde, The nucleosome family: dynamic and growing. *Structure* **17**, 160-171 (2009).
33. A. Bancaud *et al.*, Nucleosome chiral transition under positive torsional stress in single chromatin fibers. *Mol Cell* **27**, 135-147 (2007).
34. D. Kato *et al.*, Crystal structure of the overlapping dinucleosome composed of hexasome and octasome. *Science* **356**, 205-208 (2017).
35. N. P. Ulyanova, G. R. Schnitzler, Human SWI/SNF generates abundant, structurally altered dinucleosomes on polynucleosomal templates. *Mol Cell Biol* **25**, 11156-11170 (2005).
36. M. Bruno *et al.*, Histone H2A/H2B dimer exchange by ATP-dependent chromatin remodeling activities. *Mol Cell* **12**, 1599-1606 (2003).
37. M. Eltsov *et al.*, Quantitative analysis of cytoskeletal reorganization during epithelial tissue sealing by large-volume electron tomography. *Nat Cell Biol* **17**, 605-614 (2015).
38. J. A. a. H. Campos-Ortega, V., The embryonic development of Drosophila melanogaster., (1985).
39. M. D. Rand, A. L. Kearney, J. Dao, T. Clason, Permeabilization of Drosophila embryos for introduction of small molecules. *Insect Biochem Mol Biol* **40**, 792-804 (2010).
40. D. N. Mastronarde, Automated electron microscope tomography using robust prediction of specimen movements. *J Struct Biol* **152**, 36-51 (2005).
41. S. Therianos, S. Leuzinger, F. Hirth, C. S. Goodman, H. Reichert, Embryonic development of the Drosophila brain: formation of commissural and descending pathways. *Development* **121**, 3849-3860 (1995).
42. C. A. Schneider, W. S. Rasband, K. W. Eliceiri, NIH Image to ImageJ: 25 years of image analysis. *Nat Methods* **9**, 671-675 (2012).
43. A. J. Hilliker, R. Appels, A. Schalet, The genetic analysis of D. melanogaster heterochromatin. *Cell* **21**, 607-619 (1980).
44. W. J. H. Hagen, W. Wan, J. A. G. Briggs, Implementation of a cryo-electron tomography tilt-scheme optimized for high resolution subtomogram averaging. *J Struct Biol* **197**, 191-198 (2017).
45. J. Mahamid *et al.*, Visualizing the molecular sociology at the HeLa cell nuclear periphery. *Science* **351**, 969-972 (2016).
46. J. R. Kremer, D. N. Mastronarde, J. R. McIntosh, Computer visualization of three-dimensional image data using IMOD. *J Struct Biol* **116**, 71-76 (1996).
47. G. Tang *et al.*, EMAN2: an extensible image processing suite for electron microscopy. *J Struct Biol* **157**, 38-46 (2007).
48. F. Forster, R. Hegerl, Structure determination in situ by averaging of tomograms. *Methods Cell Biol* **79**, 741-767 (2007).
49. C. R. Clapier *et al.*, Structure of the Drosophila nucleosome core particle highlights evolutionary constraints on the H2A-H2B histone dimer. *Proteins* **71**, 1-7 (2008).
50. E. F. Pettersen *et al.*, UCSF ChimeraX: Structure visualization for researchers, educators, and developers. *Protein Sci* **30**, 70-82 (2021).
51. D. Lariviere *et al.*, A User-Friendly DNA Modeling Software for the Interpretation of Cryo-Electron Microscopy Data. *Methods Mol Biol* **1624**, 193-210 (2017).
52. S. M. M. Rappaport, S.; Rabin,Y., https://arxiv.org/abs/0801.3183. (2008).

53. J. L. Hodges, The significance probability of the smirnov two-sample test. *Arkiv för Matematik* **3**, 469-486 (1958).
54. E. D. Jones, T. E. Oliphant, P. Peterson. SciPy: Open source scientific tools for Python. (2001).
55. P. Carrivain, M. Barbi, J. M. Victor, In silico single-molecule manipulation of DNA with rigid body dynamics. *PLoS Comput Biol* **10**, e1003456 (2014).
56. K. Luger, M. L. Dechassa, D. J. Tremethick, New insights into nucleosome and chromatin structure: an ordered state or a disordered affair? *Nat Rev Mol Cell Biol* **13**, 436-447 (2012).
57. J. Pierson, U. Ziese, M. Sani, P. J. Peters, Exploring vitreous cryo-section-induced compression at the macromolecular level using electron cryo-tomography; 80S yeast ribosomes appear unaffected. *J Struct Biol* **173**, 345-349 (2011).
58. K. Sader, D. Studer, B. Zuber, H. Gnaegi, J. Trinick, Preservation of high resolution protein structure by cryo-electron microscopy of vitreous sections. *Ultramicroscopy* **110**, 43-47 (2009).
59. S. Cai *et al.*, Cryo-ET reveals the macromolecular reorganization of S. pombe mitotic chromosomes in vivo. *Proc Natl Acad Sci U S A* **115**, 10977-10982 (2018).
60. K. Richter, H. Gnagi, J. Dubochet, A model for cryosectioning based on the morphology of vitrified ultrathin sections. *J Microsc* **163**, 19-28 (1991).
61. S. Hihara *et al.*, Local nucleosome dynamics facilitate chromatin accessibility in living mammalian cells. *Cell Rep* **2**, 1645-1656 (2012).
62. T. Weidemann *et al.*, Counting nucleosomes in living cells with a combination of fluorescence correlation spectroscopy and confocal imaging. *J Mol Biol* **334**, 229-240 (2003).
63. R. A. Crowther, D. J. DeRosier, A. Klug, The reconstruction of a three-dimensional structure from projections and its application to electron microscopy. *Proceedings of the Royal Society of London. A. Mathematical and Physical Sciences* **317**, 319-340 (1970).